PAPER

Check for updates

One-step hydrothermal preparation of Ta-doped ZnO nanorods for improving decolorization efficiency under visible light

Thi Viet Ha Luu, [ID] *[a] Ngoc Nhiem Dao,[bc] Hoang Ai Le Pham,[a] Quang Bac Nguyen,[bc] Van Cuong Nguyen [ID] [a] and Phuc Huu Dang [ID] *[d]

In this work, Ta-doped ZnO (Ta-ZnO) nanomaterials were synthesized by the hydrothermal method at different temperatures (110, 150, and 170 °C) for the photodegradation of methylene blue (MB) under visible light. Ta doping significantly affects the crystal defects, optical properties, and MB photocatalytic efficiency of ZnO materials. The optical absorption edge of Ta-ZnO 150 was redshifted compared to undoped ZnO, correlating to bandgap narrowing ($E_{gTa-ZnO}$ = 2.92 eV; E_{gZnO} = 3.07 eV), implying that Ta doped ZnO is capable of absorbing visible light. Besides, Ta-doping was the reason for enhanced blue light emission in the photoluminescence spectrum, which is related to the oxygen defect V_O^0. It is also observed in the XPS spectra, where the percentage of oxygen in the oxygen-deficient regions ($O_{531.5}$ eV) of Ta-ZnO150 is higher than that of ZnO150. It is an important factor in enhancing ZnO's photocatalytic efficiency. The MB degradation efficiency of Ta-doped ZnO reached the highest for Ta-ZnO 150 and was 2.5 times higher than ZnO under a halogen lamp (HL). Notably, the influence of hydrothermal temperature on the structural, morphological, and photoelectrochemical properties was discussed in detail. As a result, the optimal hydrothermal temperature for synthesizing the nanorod is 150 °C. Furthermore, photocatalytic experiments were also performed under simulated sunlight and natural sunlight. The nature of the photo-oxidative degradation of MB was also investigated.

1. Introduction

ZnO is a group II–VI semiconductor oxide with a wide bandgap energy (about 3.3 eV at ambient temperature), a large exciton binding energy (60 meV), and thermal, chemical, and mechanical stability. In addition, ZnO materials are relatively inexpensive, non-toxic, and biologically friendly.[1–3] Therefore, ZnO is applied in many fields, such as optics, magnetism, electronics, energy, sensors, rubber, ceramics, medicine, and catalysis.[4–6] During the past two decades, ZnO has received much research attention as a photocatalyst, and the results show that ZnO has good catalytic activity under ultraviolet light.[3,7,8] According to some reports, ZnO outperforms TiO₂ and other semiconductor oxides of photocatalytic activity, which is determined by the ability to absorb solar radiation.[9–11]

Two primary issues that limit ZnO from being utilized as a photocatalyst are its wide bandgap energy and the rapid recombination of electron pairs and photogenerated holes. Metal doping is one remediation method involving transition metals such as Mn, Co, Fe, Cu, Mg, and Ta, [12–17] and rare earth elements such as Er, Sm, La, Ce, Pr, Er, Yb into ZnO.[18–21] Because doping can change the morphology, reduce the grain size, increase the crystal defect level, and reduce the band gap energy of ZnO.[22–25] When the size of the particles decreases, the specific surface area gradually increases, thereby increasing the adsorption capacity. Also, the d and f orbitals of transition metals or rare earth elements are often empty or not filled. The interaction of the d and f orbitals with the valence or conduction band of ZnO can reduce the band gap energy and extend the optical absorption to the visible light region. In addition, the substitution of zinc ions by doped metal ions also changes the electron band structure, producing many crystal defects (*i.e.*, V_{Zn}, V_O). The oxygen-hole (V_O) defect can effectively act as an electron "trap," thereby minimizing the photogenerated electron and hole recombination. Transition metal Ta has many oxidation states (*i.e.*, +3, +4, +5). The radius of Ta⁵⁺ (0.64 Å), Ta⁴⁺ (0.68 Å), and Ta³⁺ (0.72 Å) ions are close to the radius of Zn²⁺ ion (0.74 Å). So, in theory, Ta ions can replace efficiently with Zn

[a]Faculty of Chemical Engineering, Industrial University of Ho Chi Minh City, Ho Chi Minh City, 700000, Vietnam. E-mail: luuthivietha@iuh.edu.vn

[b]Institute of Materials Science, Vietnam Academy of Science and Technology, 18 Hoang Quoc Viet, Hanoi, 100000, Vietnam

[c]Graduate University of Science and Technology, Vietnam Academy of Science and Technology, 18 Hoang Quoc Viet, Hanoi, 100000, Vietnam

[d]Faculty of Fundamental Science, Industrial University of Ho Chi Minh City, Ho Chi Minh City, 700000, Vietnam. E-mail: danghuuphuc@iuh.edu.vn

ions in the ZnO lattice, and a little Ta doping content would be needed to provide more free carriers.

Up to now, the reports on Ta doped ZnO are quite a few, and they only focus on materials' electrical, thermal, and optical properties.[26–32] Some other reports study antibacterial or catalytic properties,[33,34] and there are very few research reports on the photocatalytic activity of Ta-doped ZnO.[16,17] In a study by the author group B.-L. Guo with colleagues, Ta-doped ZnO nanomaterials were prepared by a modified Pechini-type method, and their antibacterial ability was studied with some Gram-positive bacteria *Bacillus subtilis* (*B. subtilis*) and *Staphylococcus aureus* (*S. aureus*) and *Escherichia coli* (*E. coli*) Gram-negative and *Pseudomonas aeruginosa* (*P. aeruginosa*).[35] The results showed that Ta-doping concentrations affecting the minimum inhibitory concentrations (MICs) of different bacteria in the dark were evaluated. The MIC results indicated that doping Ta^{5+} ions into ZnO significantly improved the bacteriostatic effect of ZnO nanoparticles on *E. coli*, *S. aureus*, and *B. subtilis* in the absence of light. Moreover, compared with the MIC results of Ta-doped ZnO and undoped ZnO nanoparticles showed a much stronger bactericidal effect on *P. aeruginosa*, *E. coli*, and *S. aureus* under visible light. Based on antibacterial tests, 5% Ta-doped ZnO is a more effective antibacterial agent than pure ZnO. In the other J. Z. Kong *et al.*, Ta-ZnO (0–4% mol) nanoparticles were synthesized by an improved polymerization complexation method for MB decomposition reactions under visible light.[16,17] The results showed that the 1% Ta-doped ZnO gave the highest MB decomposition efficiency and reached over 95% after 50 minutes of irradiation under visible light and higher than ZnO undoped. Improving in photocatalytic activity of Ta-doped ZnO nanoparticles was suggested that the photodegradation of methylene blue under visible light irradiation depends on the content of the Ta doping, which can impact the size of the particles, the number of hydroxyl groups on the surface, the number of active hydrogen-related defect sites, and visible-light absorption.

In our work, Ta-doped ZnO material was synthesized by a simple hydrothermal method at different hydrothermal temperatures. The precursors were zinc acetate, tantalum(v) chloride, ethanol as a solvent, and an alkaline medium. The influence of temperature on the structure, morphology, photoelectric properties, and photocatalytic activity of Ta-doped ZnO materials has been studied and discussed in detail. Besides, photocatalytic experiments under simulated sunlight, natural sunlight, and the nature of photooxidative decomposition of MB were also studied.

2. Materials and Methods

2.1 Materials

All chemicals, including $Zn(CH_3COO)_2 \cdot 2H_2O$, $TaCl_5$, C_2H_5OH, NaOH, and methylene blue were purchased without further purification from Shanghai Aladdin Bio-Chem Technology Co., Ltd. Silver nitrate ($AgNO_3$, 99.9%), ethylenediamine tetra acetic acid (EDTA, >99%), isopropanol (99.5%), and 1,4-benzoquinone (98%) were purchased from Merck.

2.2 Synthesis of Ta-ZnO by hydrothermal method

Ta-ZnO materials were synthesized by a hydrothermal method with precursors of zinc acetate ($Zn(CH_3COO)_2$), tantalum chloride ($TaCl_5$), solvent C_2H_5OH, and strong alkaline medium (NaOH). The Ta-ZnO110, Ta-ZnO150, and Ta-ZnO170 were prepared with the molar ratio of Ta^{5+}/Zn^{2+} = 2% at different hydrothermal temperatures of 110 °C, 150 °C, and 170 °C, respectively. To begin, dissolve 1.098 g $Zn(CH_3COO)_2$ and 0.036 g $TaCl_5$ in 80 ml C_2H_5OH. The solution was then slowly added to 70 ml of 0.5 M NaOH and stirred for 90 minutes. The mixtures were then put in an autoclave and kept warm in an oven for 20 hours at a specific temperature. After that, the autoclave was allowed to reach room temperature. The solution was then removed by washing and ethanol several times before it was filtered through Whatman No. 1 filter paper. Finally, the solid is dried for 12 hours at 85 °C to produce the Ta-ZnO powder.

2.3 Research methods on material properties

Various surface analyses were used to study the properties of the synthesized materials. X-ray diffraction (XRD) patterns were analyzed by the D8 Advance XRD (Bruker, Germany) system at wavelengths λ = 1.5406 Å. Scherrer's formula was used to calculate the average crystal size (eqn (1)):

$$D = \frac{0.9\lambda}{\Delta(2\theta) \times \cos\theta} \tag{1}$$

where: – D: average crystal size; – λ: wavelength of X-ray (1.5406 Å); – $\Delta(2\theta)$ = FWHM: full width of half maximum.

The lattice constant is identified by the formula (eqn (2)):

$$\frac{1}{d_{(hkl)}^2} = \left[\frac{4}{3}\left(h^2 + k^2 + hk\right) + l^2\frac{a^2}{c^2} \right] \frac{1}{a^2} \tag{2}$$

Where d is the spacing between planes of given Miller indices h, k, and l; a, b, and c are the lattice constants.

FT-IR spectrometer was studied at PerkinElmer (USA). The scanning electron microscope was used to investigate the material's surface morphology (Hitachi S-4800, Japan). The UV-vis absorption spectra were obtained using diffuse reflectance spectroscopy (DRS, V-500 Jasco, Japan). Photoluminescence spectra were obtained using a 355 nm excitation wavelength on a Horiba HQ iHR550. The PHI Quantera SXM (ULVAC-PHI, Japan) PHI X-ray optoelectronic device with a monochrome X-ray source of Al Kα (1486.6 eV) was used to analyze the elemental composition and surface chemical properties of synthesized materials. The photocurrent and EIS spectrums were analyzed for photoelectrochemical properties (BioLogic SP-240). The materials were pasted into the working electrode. Three electrodes were put in 0.1 M Na_2SO_4 electrolyte under a Philips 150 W halogen lamp, including a Pt wire counter electrode and an Ag/AgCl (3 M KCl) reference electrode.

2.4 The photocatalytic activity of Ta-ZnO under visible light

MB degradation under visible light was employed to determine the photocatalytic activity of Ta doped ZnO. The concentration

of MB remaining over time was measured on a UV-VIS Evolution 600 Thermo Fisher device (USA). The irradiated light source for the photochemical reaction was the Philips 150 W halogen lamp (HL, 100 mW cm^{-2}), simulated sunlight (SSL, mercury vapor lamps 450 W (U.S.A), 100 mW cm^{-2}), and sunlight (SL, 78 000–90000 lux).

A mixture of 0.05 g Ta-ZnO and 100 ml of a 7 ppm MB solution was stirred in the dark for 90 min on a magnetic stirrer to achieve adsorption equilibrium. The reaction solution was then taken out in 3 ml portions and centrifuged to separate the catalyst. The optical density was measured by Uv-vis spectrophotometry (time $t = 0$, optical density A_o). After that, the solution was stirred under visible light (HL) irradiation. Every 30 minutes, 3 ml of solution was centrifuged to separate the solids, and the optical density (A_t) was measured. The formula determined the MB decomposition efficiency (H%) (eqn (3)):

$$H(\%) = \frac{C_0 - C_t}{C_0} \times 100\% = \frac{A_0 - A_t}{A_0} \times 100\% \qquad (3)$$

Where A_t and A_0 are the optical density of MB at the peak at 664 nm at $t = 0$ and t min, respectively. C_t and C_0 are the concentration of MB at $t = 0$ and t min, respectively.

The investigation of photo-oxidative species trapping was conducted to understand them in MB decolorization process. Scavengers were added such as silver nitrate (AgNO$_3$, catch e$^-$), EDTA (catch h^+), isopropanol (Isopr, catch $\cdot$OH), and 1,4-benzoquinone (p-BQ, catch $\cdot$O$_2^-$).[36–38] The reduction of MB solution was related the contribution of active species. In our study, 1 mM scavengers were added to the reactive solution before illumination.

3. Results and discussions

3.1 XRD results

The structure and crystal phase characteristics of Ta-doped ZnO synthesized at different hydrothermal temperatures were investigated using X-ray diffraction (XRD), shown in Fig. 1. Fig. 1A shows that all samples Ta-ZnO110, Ta-ZnO150, and Ta-ZnO170 display the hexagonal wurtzite structure of ZnO with high and sharp diffraction peaks of lattice planes (100), (002), (101), (102), (110), (103), (200), (112), and (201), respectively. This result is consistent with the ZnO wurtzite hexagonal structure according to JCPDS standard 00-036-1451. However, diffraction angles

slightly shift toward the two-theta angle smaller than the undoped ZnO (Fig. 1B). It can be seen that the Ta-doped ZnO crystals are formed from 110 °C to 170 °C. At high spontaneous pressure and temperature (110–150 °C), ions Ta can enter ZnO lattice defects or partially displace the zinc ions in hydrothermal conditions. Notable, the Ta-ZnO170 pattern presents two more phases, including the ZnTa$_2$O$_6$ orthorhombic phase with small diffraction peaks at 52.80 and 58.30 (JCPDS 39-1484) and the Ta$_2$O$_5$ orthorhombic phase with a diffraction peak at 32.60 (JCPDS 71-0639). This is due to the hydrothermal synthesis temperature affecting the crystalline phase formation of Ta-doped ZnO materials. The temperature increases to 170 °C, and the autogenous pressure also increases, which can be thermodynamically favorable for forming Ta$_2$O$_5$ and ZnTa$_2$O$_6$ phases. These phases were also observed in the work of D. Richard et al.[39] Doping 2% Ta into ZnO by the sol–gel method with an annealing temperature of 400–600 °C gave a single-phase structure. However, the orthorhombic phases Ta$_2$O$_5$ and ZnTa$_2$O$_6$ appeared when the annealing temperature increased to 800 °C.[39]

The crystal size and lattice parameters of Ta-doped ZnO materials were calculated and shown in Table 1. The result shows that the lattice constants of Ta-ZnO110 and Ta-ZnO150 slightly decrease and that of Ta-ZnO170 slightly increases compared to undoped ZnO. However, the c/a ratio of all is still approximately 1.6. The Ta-doped ZnO synthesized at 150 °C is the smallest crystal size.

3.2 SEM images

The material morphology of samples ZnO-150, Ta-ZnO110, Ta-ZnO150, and Ta-ZnO170 are shown in SEM images (Fig. 2).

Table 1 Lattice parameters and crystal sizes of ZnO150, Ta-ZnO110, Ta-ZnO150

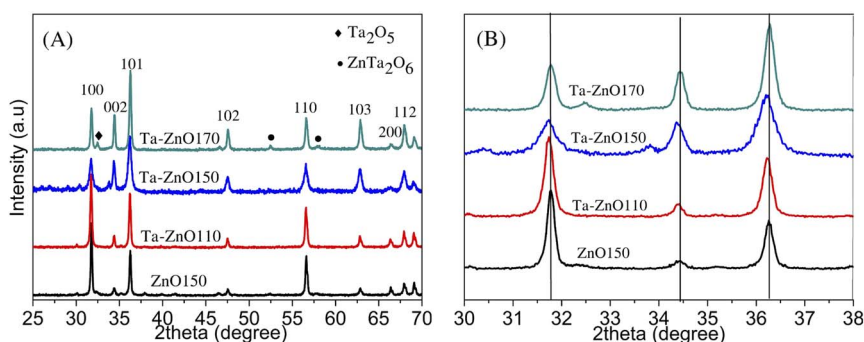| Samples	Crystal size (nm)	Lattice parameters (Å)			
		a	b	c	c/a
Ta-ZnO110	33.39	3.2509	3.2509	5.2106	1.603
Ta-ZnO150	26.85	3.2469	3.2469	5.2056	1.603
Ta-ZnO170	39.82	3.2565	3.2565	5.2165	1.602
ZnO150	45.91	3.255	3.255	5.2091	1.600

Fig. 1 XRD pattern of (A) ZnO150 and Ta doped-ZnO synthesized with different hydrothermal temperatures (B) magnified view of the XRD pattern with 2θ range from 30° to 38°.
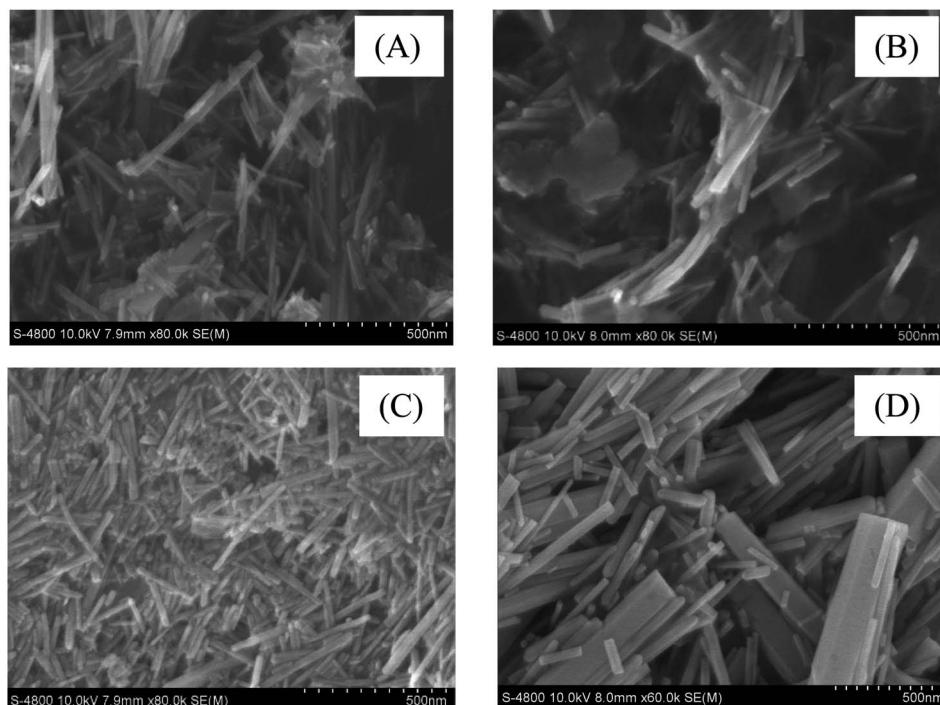
Fig. 2   SEM images (A) ZnO150, (B) Ta-ZnO110, (C) Ta-ZnO150 and (D) Ta-ZnO170.

This fig shows that Ta-ZnO110 materials are heterogeneous shapes, including long rods and flat plates (Fig. 2B), and Ta-ZnO150 materials are relatively uniform long rod shape with a width of about 25–50 nm (Fig. 2C). The Ta-ZnO170 material is rod-shaped, 35–200 nm in width, but irregular, with the broken rods. It can be shown that Ta-ZnO110 nanorod crystals can be formed at 110 °C; however, the spontaneous pressure is not thermodynamically strong enough for the reactions to occur ultimately, so the part remains in the form of a flattened array that cannot be separated into individual rods. On the contrary, at 170 °C, high spontaneous pressure is thermodynamically favorable to forming Ta-ZnO170 nanorod crystals. However, these rods are easy to aggregate and form larger-sized rods. Besides, the small rods are easily broken due to the fast and powerful thermal movement in the synthesis progress. In summary, the hydrothermal temperature of 150 °C is an appropriate temperature to synthesize both ZnO and Ta-ZnO materials with a more uniform rod shape and smaller size.

3.3   XPS results

The XPS results were studied to learn more about the existence and oxidation states of as-produced materials. Ta4d, Zn2p, O1s, and C1s XPS peaks were calibrated by the C1s peak (284.8 eV). Zn and O elements are observable in all samples, and Ta is also detected in Ta-ZnO150, as shown in Fig. 3. Fig. 3B displays two symmetric $Zn2p_{3/2}$ and $Zn2p_{1/2}$ peaks for ZnO150 at 1021.3 and 1044.4 eV, which show a chemical state of Zn^{2+}.[28] However, in Ta-ZnO150, these peaks are shifted lower in their locations. In more clear terms, $Zn2p_{3/2}$ peak was found to be at 1022 eV, while $Zn2p_{1/2}$ peak was found to be at 1045 eV. It is due to the substitution of ion Zn^{2+} by ion Ta^{5+} and the addition of Zn–O–Ta binding energy, as mentioned in the XRD results. Typical peaks of Ta were $Ta4d_{5/2}$ and $Ta4d_{3/2}$ (Fig. 3D), observed at 230.5 and 242.1 eV, respectively. The atomic contents are determined based on the O1s core-level peak, which is further deconvoluted into three subpeaks: one at 530.8 eV, which is attributed to the Zn–O bond and assigned $O_{530.8}$, and another at 531.5 eV, which is attributed to the O of the Zn–O bond in oxygen-deficient regions and assigned $O_{531.5}$. The other peak at 532.5 eV was attributed to the O^{2-} ion of surface chemisorbed oxygen.[40] Notably, Ta-ZnO15 have a higher percentage of $O_{531.5}$ than ZnO150 (Table 2). It implies that the oxygen vacancies on the ZnO surface as it was originally made increased after doping, which could be partially accounted for by the band gap results.

3.4   FT-IR spectra

Fig. 4 depicts the infrared spectra of Ta-doped ZnO and undoped ZnO. The broadband at around 3460 cm^{-1} corresponds to the vibration of O–H due to the surface adsorption of water.[41] The weak peaks are near 1630 cm^{-1}, the location of the corresponding H–O–H bending vibration. Notably, the adsorption peaks from 400–600 cm^{-1} are typical for metal–oxygen bonds (Zn–O, Zn–O–Ta).[16] In addition, Ta-ZnO110 has the presence of absorption peaks at 875, 1078, 1427, and 1540 cm^{-1}, which characterize the bond vibrations C–H, C–O–C, C=O, and (COO−), respectively, due to the hydrothermal reaction to form Ta-ZnO crystals occurs incompletely at 110 °C.[41–46] These peaks disappear with the Ta-ZnO150 and the Ta-ZnO170 °C. This result is consistent with the SEM results discussed above. The XRD, SEM, and FT-IR research results show that 150 °C is
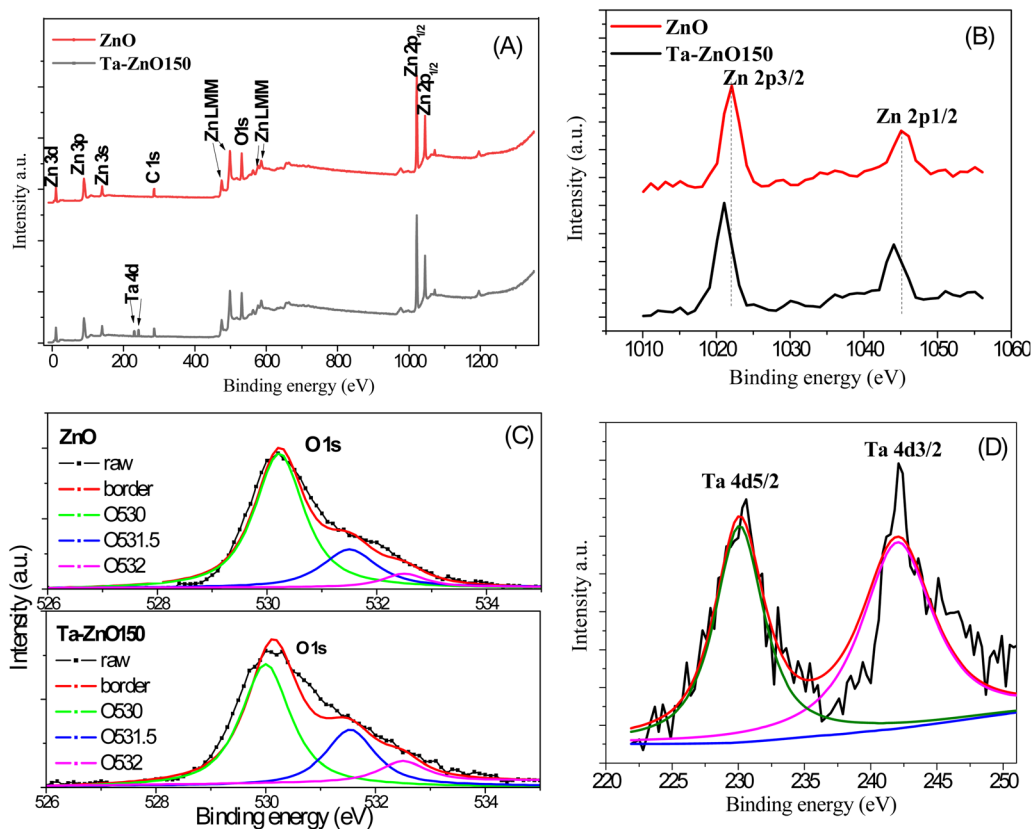
Fig. 3 (A) Survey XPS spectra and XPS spectra of (B) Zn2p, (C) Ta3d, and (D) O1s of Ta-ZnO150 and ZnO150.

Table 2 XPS results for the atomic content (%) of the Ta-ZnO150 and ZnO150

Atomic content (%)	Ta-ZnO150	ZnO150
Zn	50.21	51.19
O_{530}	34.75	37.85
$O_{531.5}$ (V_O)	12.88	10.96
Ta	2.38	—

a suitable for hydrothermal synthesis of Ta-doped ZnO nanorods.

3.5 UV-vis-DRS results

The optical properties of Ta-ZnO150 and ZnO150 nanorods were studied using the UV-vis spectroscopy. The bandgap energy was determined based on optical density data obtained– by the Tauc method.[47,48] In this method, the graph represents the relationship between $(\alpha h\nu)^{1/n}$ and the energy $(h\nu)$ according to the equation: $(\alpha h\nu)^{1/2} = B(h\nu - E_g)$. In which: α, h, ν, B, and E_g are the absorption coefficient, Planck constant, frequency of the photon, rate constant, and band gap, respectively. α–Absorption coefficient is calculated according to the equation: $\alpha = 2.303 \times \dfrac{A}{t}$ or $\alpha = \dfrac{1}{L}\ln T$. Where A, T, L, and t are optical density, transmittance, sample thickness (cuvette), and film thickness, respectively. A relationship between A and T
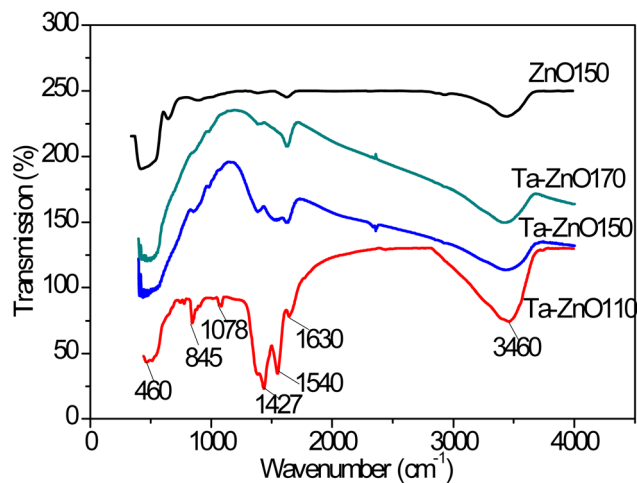

Fig. 4 FT-IR spectra of ZnO150, Ta-ZnO110, Ta-ZnO150, and Ta-ZnO170.

expresses $A = \log(1/T)$. The results of the optical absorption spectrum and the graph showing the correlation between $(\alpha h\nu)^{1/2}$ with the energy $(h\nu)$ by the Tauc method are shown in Fig. 5. This result shows that the optical absorption edge of Ta-ZnO150 nanorods shifts toward a longer wavelength than that of ZnO150 (Fig. 5A), which relates to the decreasing Ta-ZnO150 band gap energy (2.92 eV) compared to undoped (3.07 eV). Thus, Ta doping significantly reduced (0.15 eV) the band gap
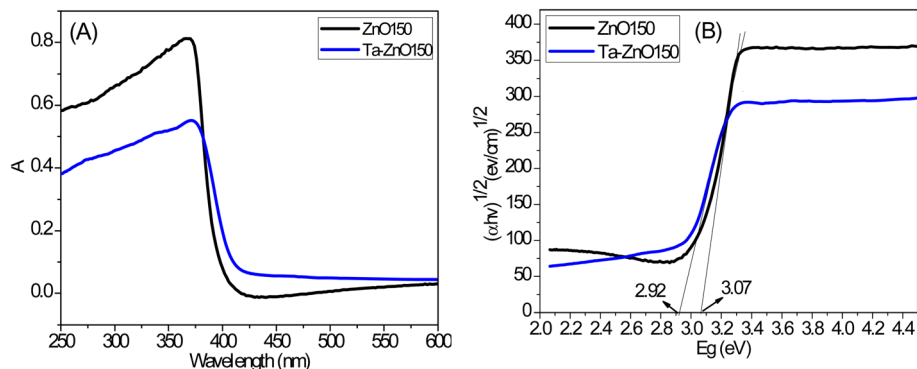
Fig. 5 (A) UV-vis spectra of Ta-ZnO150 and ZnO150; (B) band gaps from Tauc of Ta-ZnO150 and ZnO150.

Table 3 The bandgap energy and the optical absorption wavelength of the materials

Samples	E_g (eV)	λ (nm)
ZnO150	3.07	403
Ta-ZnO150	2.92	425

energy of ZnO and increased optical absorption in the visible light region (Table 3). The narrowing of the band gap of ZnO upon Ta doping was also reported by S. Pat et al.[32] and R. Althaf et al.[27] R. Althaf et al. proposed that a new band gap is formed inside the ZnO band gap and right on top of the conduction band due to the hybridization of Ta d orbitals and the strong sp-d interaction of O_{2p} and Ta_{5d}. As a result, the conduction band is enlarged, and the band gap is narrowed. Besides, the study of Y. Wu et al. explained the decrease in band gap energy due to the increase of lattice defects (oxygen holes, zinc holes, interstitial zinc, interstitial oxygen, etc.) in ZnO.[28] These defects form local energy levels inside the band gap, leading to shifting the optical absorption region to the visible light region.[28]

3.6 PL result

Luminescence (PL) spectroscopy is an appropriate technique for investigating the crystallinity, presence of impurities, defects, and electron–hole recombination processes of materials.[49,50] Fig. 6 depicts the PL spectra of Ta-ZnO and ZnO materials at room temperature with an excitation wavelength of 355 nm. There are two peaks in the UV and visible regions, in which the UV peak in the PL spectrum is related to the near band edge emission (NBE), and the emission peaks in the visible region are usually derived from defects in the crystal structure.[51] Besides, the intensity of the 390 nm UV peak relates to the electron–hole recombination rate, which significantly affects the photocatalytic properties of the material. In this case, the UV emission peak intensity of the Ta-ZnO150 material is reduced compared to that of the undoped ZnO material. This reduction may be due to Ta doping increasing the point defects in the ZnO lattice. Therefore, the electron emission after being excited emits low energy, and the lifetime of the electron is longer because there is a small energy transition in the band
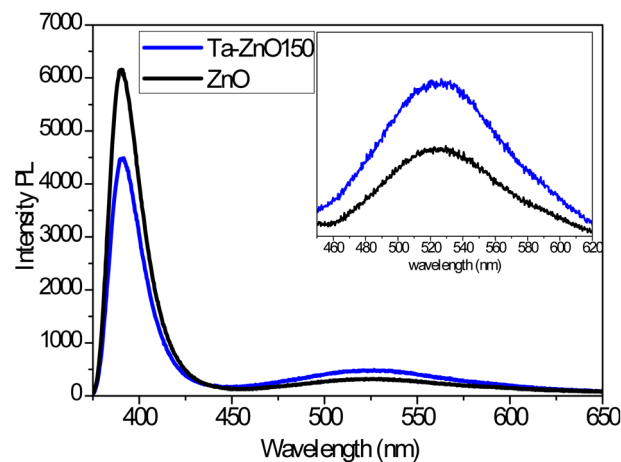

Fig. 6 PL spectra of Ta-ZnO150 and pure ZnO.

gap before returning to the valence band. As a result, Ta doping has reduced the electron–hole recombination rate of ZnO materials.

In addition, the PL results also show that the broad emission peaks with low intensity in the visible light region (450–650 nm) relate to oxygen hole defects in the crystal structure.[52,53] According to these works, this emission corresponds to the transition of electrons from the singly ionized oxygen vacancies or the shallow donor (interstitial zinc) to the valence band or the conduction band.[26,52] The intensity emission of Ta-ZnO150 material is higher than that of undoped ZnO150 material. In our case, it is proposed that the substitution of ion Zn^{2+} by ion Ta^{5+} is responsible for increasing the density of defects such as oxygen vacancies and interstitial zinc. This result agrees with the previously mentioned XPS result. The oxygen vacancy defect is beneficial for photocatalysis as a mediator for transporting electrons and energy from the catalyst to the pollutant, thereby limiting the electron recombination process (photogenic holes) and accelerating the decomposition of organic matter.[17] Our research results are almost similar to the research results of V. Herrera et al.[26] Based on these results, we can say that the doping method has a significant effect on the types and amounts of defects in the ZnO nanostructures, which changes

the energy structure in the band gap and makes the photocatalytic activity better.

3.7 Photo-electrochemical results

The recombination rate of photogenerated electron–hole pairs, the interfacial contact layer resistance, and other parameters can be verified using the EIS measurement, as shown in Fig. 7A. The charge transfer resistances (R_{ct}) for ZnO, Ta-ZnO110, Ta-ZnO150, and Ta-ZnO170 samples were calculated as 3542, 3106, 2141, and 2601 Ω, respectively. These Rct values suggest that photogenerated electron-hole pairs are separated from carriers in Ta-ZnO150 more effectively and at a faster rate. Photocatalysts' transient photocurrent responses were used to confirm the separation of charge carrier pairs and how the catalyst reacts to light. During on/off switching cycles, the photo responses of ZnO, Ta-ZnO110, Ta-ZnO150, and Ta-ZnO170 were tested under visible light. It is realized that under visible-light irradiation, the photocurrent of Ta-ZnO150 NRs (achieved at 4.9 μA cm^{-2} at 0.3 V *versus* $V_{Ag/AgCl}$) is almost 3.5 times higher than that of ZnO NRs (1.4 μA cm^{-2} at 0.3 V *versus* $V_{Ag/AgCl}$). In addition, Ta-ZnO NRs' photocurrent remains unchanged even after five cycles of light-on/light-off. It can be proved that the Ta doping of ZnO has improved the separation and transfer of the photogenerated charge, according to the photocurrent density and PL measurements.

3.8 Photocatalytic activity result

The photocatalytic activity of the synthesized Ta-ZnO materials at different hydrothermal temperatures was studied through the MB decomposition reaction under visible light (HL). The results in Fig. 8A show that after 120 minutes of irradiation, the MB degradation efficiency was 77.0%, 87.0%, 97.8%, and 92.8% for ZnO, Ta-ZnO110, Ta-ZnO150, and Ta-ZnO170 samples, respectively. Thus, the decrease in MB concentration for all Ta-doped ZnO samples is higher than that for undoped samples, of which Ta-ZnO150 has the highest. The reaction kinetics were also studied by plotting the correlation $\ln(C_0/C_t)$ *versus* time. Fig. 8B shows good linearity between $\ln(C_0/C_t)$ *versus* time for all samples, with regression coefficient R^2 values close to 1. It

indicates that the MB degradation reactions under visible light follow a first-order kinetic model.

The reaction rate constants for catalysts are as follows: ZnO < Ta-ZnO110 < Ta-ZnO170 < Ta-ZnO150, and the reaction rate with Ta-ZnO150 catalyst is approximately 2.5 times higher than ZnO catalyst (Table 4). Ta doping increases the photocatalytic efficiency of ZnO which is explained that Ta doping reduced the band gap energy (decreased 0.15 eV), thereby increasing the optical absorption of the visible light region of ZnO. Beside, Ta doping also increases the lattice defects, including the oxygen hole defect, which is an essential contribution in greatly reducing the electron–hole recombination rate, thus increasing the quantum efficiency for MB decomposition.

Moreover, the effect of hydrothermal temperature on the MB decolorization efficiency of materials can be related to the crystal quality, morphology, and defect concentration. The MB decomposition efficiency of Ta-ZnO110 materials at the hydrothermal temperature of 110 °C is the lowest because the crystals of Ta-ZnO110 can be formed with low crystallinity (XRD) and heterogeneous shapes, including rods and flat arrays (SEM). In contrast, at the high hydrothermal temperature of 170 °C, the Ta-ZnO170 nanorods formed well with crystallinity, but the larger nanorods size, thus the specific surface area of the material reduced. Besides, at a high hydrothermal temperature of 170 °C, there are the formation phases of Ta_2O_5 and $ZnTa_2O_6$, which reduce the concentration of Ta^{5+} in the ZnO lattice, thereby reducing electron conduction and oxygen-hole defect concentration. From this result, the catalyst material Ta-ZnO150 will be used for further experiments. The effects of doping on the defect concentration and photocatalytic efficiency were also observed in these studies.[54,55]

The catalytic activity of Ta-doped ZnO materials was also tested under simulated sunlight and sunlight, as shown in Fig. 8F shows that the MB decomposition efficiency after 60 minutes is 96.7%, 89.2%, and 79.6% for sunlight, simulated sunlight, and halogen lamp, respectively, and the MB decomposition efficiency under sunlight is the highest. As discussed above, the band gap energy of Ta-ZnO150 material was determined to be approximately 2.92 eV, corresponding to the optical absorption wavelength region $\lambda \leq 425$ nm. As a result, Ta-ZnO150 absorbs UV light and a portion of visible light very
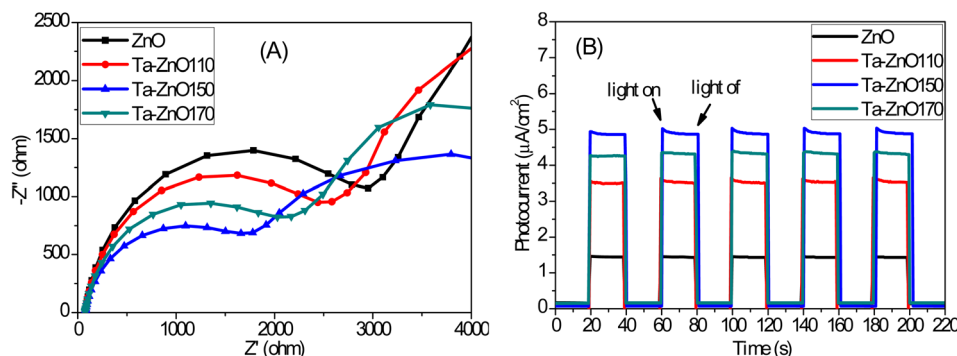

Fig. 7 (A) Electrochemical impedance spectroscopy (EIS) Nyquist plots and (B) transient photocurrent responses of, ZnO150, Ta-ZnO110, Ta-ZnO150, and Ta-ZnO170.
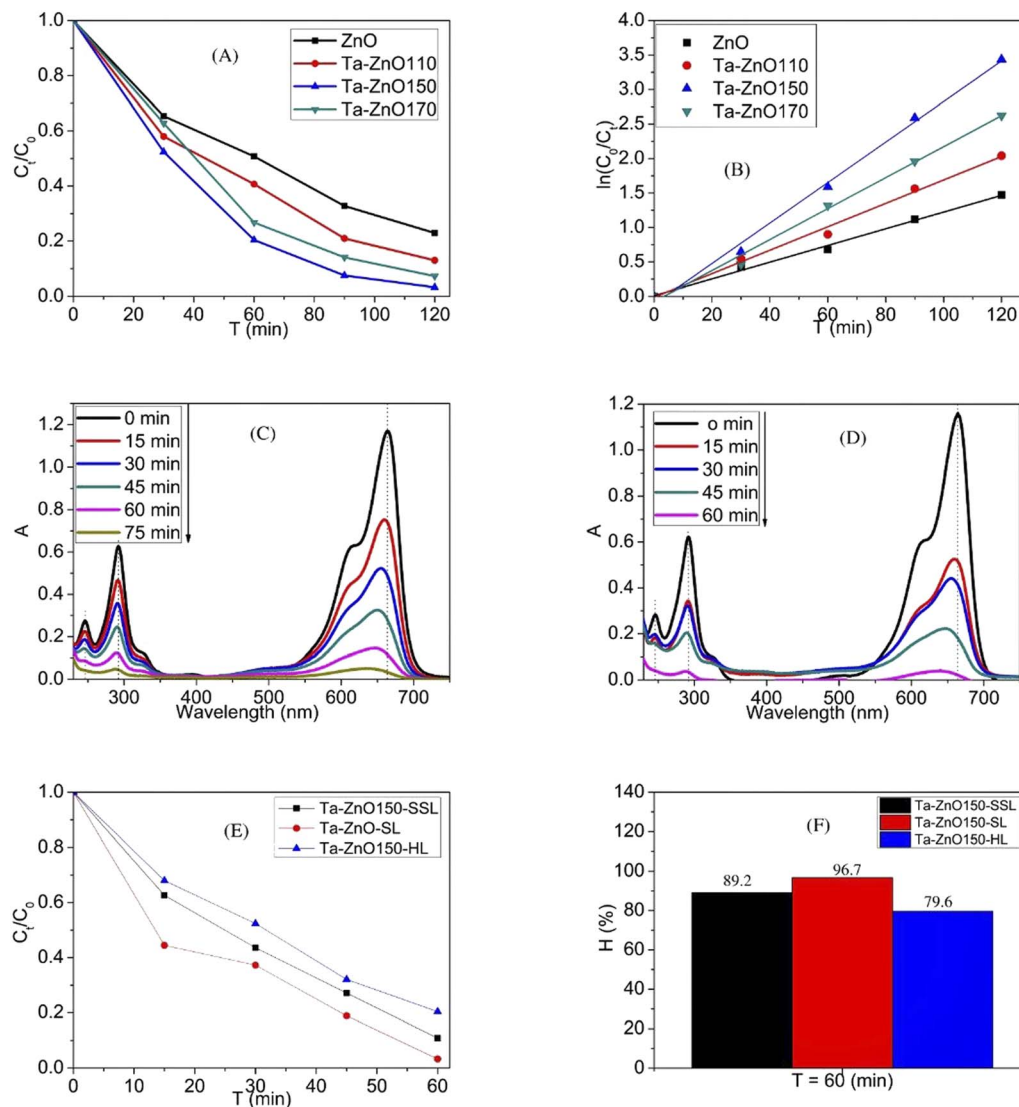
Fig. 8 (A) and (B) MB decomposition of Ta-ZnO110, Ta-ZnO150, and Ta-ZnO170 under Philip 150 W halogen lamp (HL); (C) and (D) MB decomposition of Ta-ZnO150 under simulated sunlight (SSL), and sunlight (SL); (E) and (F) Comparison of MB degradation and MB degradation efficiency of Ta-ZnO150 materials.

Table 4 First-order kinetics of MB decomposition reaction of Ta-doped ZnO materials

	Kinetic equations of order 1	k (min^{-1})	R^2
ZnO	$y = 0.012 \times + 0.0109$	0.012	0.9951
Ta-ZnO110	$y = 0.017 \times - 0.0106$	0.017	0.9938
Ta-ZnO150	$y = 0.0294 \times - 0.1105$	0.0294	0.9955
Ta-ZnO170	$y = 0.0225 \times - 0.075$	0.0225	0.9943

well. Moreover, sunlight or simulated illumination gives even higher MB decomposition efficiency because it includes UV rays (about 5%) and visible light. This result partly shows the significance of doping Ta in ZnO with the desire to narrow its bandgap energy, increase the optical absorption capacity of the visible light region, and expand the applicability of ZnO.

Liquid total organic carbon (TOC) of samples was determined on a Shimadzu TOC-VCPH analyzer (Japan) to measure the amount of carbon found in the dye that was degraded to CO_2 during oxidation. The results in Table 5 show that, after 1 hour of irradiation, the TOC mineralization efficiency of MB solution reached 88.07% and 75.56% for sunlight simulating lamp and halogen lamp, respectively. The mineralization efficiency under sunlight-simulated lamp irradiation is higher than that of a halogen lamp and approximates MB degradation efficiency (89.2%). Thus, it can be seen that the Ta-ZnO150 material effectively mineralizes methylene blue dye under visible light.

The role of the reaction species in the MB decomposition progress was evaluated by adding capture agents, such as Isopr (capture $^{\cdot}$OH), OA (capture h$^+$), p-BQ (capture $^{\cdot}O^{2-}$), and AgNO$_3$ (capture e$^-$) (Fig. 9). They were added to the reaction solution at a concentration of 1 mM after stirring in the dark to

Table 5 The MB degradation efficiency and TOC mineralize efficiency under illumination Halogen lamp and Sunlight-simulated lamp of Ta-ZnO150 after 60 min

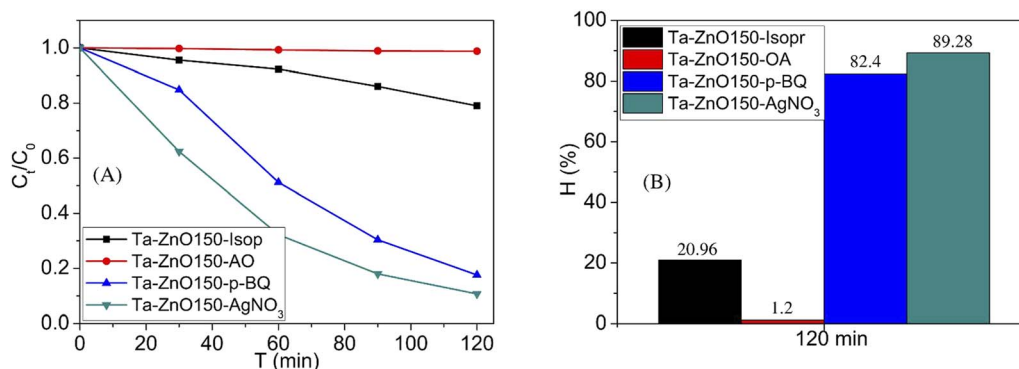|	MB			TOC		
Light illumination	Initial (mg L^{-1})	Final (mg L^{-1})	H (%)	Initial (mg L^{-1})	Final (mg L^{-1})	H (%)
SSL	5.95	0.6426	89.2	3.52	0.42	88.07
HL	5.95	1.214	79.6	3.52	0.86	75.56

Fig. 9 Effect of radical scavenging agents on (A) the MB degradation during 120 min and (B) MB degradation efficiency at 120 min of Ta-ZnO150 catalyst under visible light (HL).

achieve adsorption equilibrium and turn on the light.[19] Fig. 9 displays that the concentration of MB decreased significantly with adding p-BQ and AgNO$_3$, decreased slightly with adding isopropanol, and was almost unchanged with adding AO. In detail, MB decomposition efficiency after 120 minutes reached 20.96, 1.2, 82.4, and 89.28% with adding isopropanol, AO, p-BQ, and AgNO$_3$, respectively. That implies that OH and h$^+$ are the main contributors to MB photodegradation, and the progress includes photooxidation reactions. Accordingly, the roles of the

pieces are arranged in order: e$^-$ < ˙O$_2$$^-$ < ˙OH < h$^+$. The photocatalytic reaction mechanism relates to the transfer of photogenerated electrons, holes, and the energy levels of the conduction and valence bands of the semiconductor. The conduction and valence band energies are calculated according to the following (eqn (4) and (5)).[56]
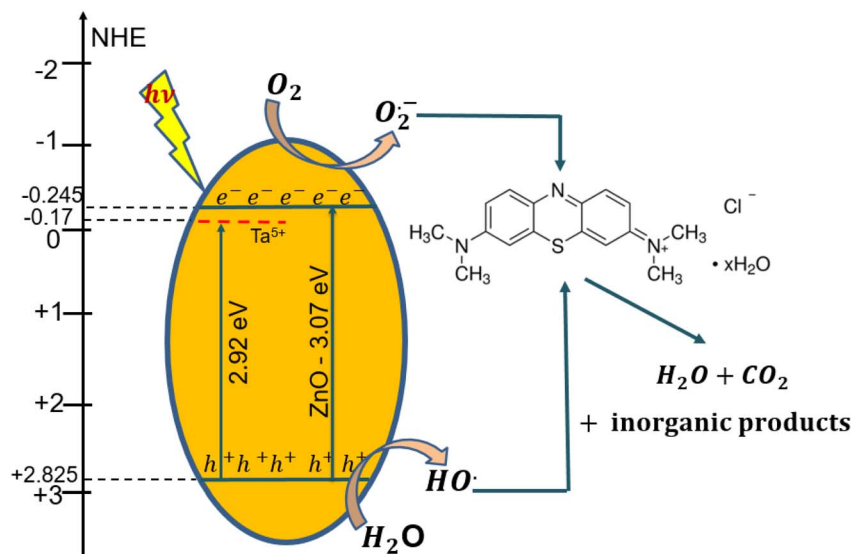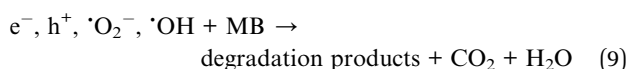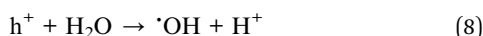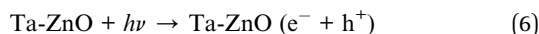
$$E_{VB} = \chi - E^c + 0.5 E_g \qquad (4)$$

Fig. 10 The mechanism proposed for MB degradation reaction of Ta–ZnO catalyst under visible light.

$$E_{CB} = E_{VB} - E_g \qquad (5)$$

where: E^c is the free electron energy on the hydrogen electrode scale (4.5 eV), E_{CB} is the conduction band energy, E_{VB} is the valence band energy, E_g is the band gap energy of ZnO, χ is the negative electron of ZnO in Mulliken: $\chi_{ZnO} = (\chi_{Zn}.\chi_O)^{1/2} = 5.79$ eV.

Based on of UV-vis spectrum, the band gap energy of Ta-ZnO150 is determined to be 2.92 eV (Table 3), so the E_{VB} and E_{CB} energy values of Ta-ZnO150 are calculated as 2.75 and −0.17 eV, respectively.

The proposed reaction mechanism is shown in Fig. 10. After irradiating, the electron in the valence band of Ta-ZnO150 receives energy ($h\nu$), transfers to the conduction band, and leaves a hole in the valence band (eqn (6)). The photoexcited electron (e^-) can reduce from +0.5 to −1.5 V, and the photo-generated hole can oxidize from +1.0 to +3.5 V, so when the electron transfer on the catalyst surface, it can react with O_2 produces $^{\bullet}O_2^-$ radicals ($E^0_{O_2/{\cdot}O_2^-}$ from −0.16 and −0.33 V) (eqn (7)), while h^+ can react with water 18 molecules to produce $^{\bullet}OH$ radicals ($E^0_{\cdot OH/H_2O} = +2.31$) (eqn (8)).[57] The agents as h^+, e^-, $^{\bullet}O_2^-$, $^{\bullet}OH$ are very strong reducing and oxidizing agents, capable of completely decomposing and mineralizing MB to produce CO_2, H_2O, and less toxic inorganic products (eqn (9)).

$$Ta\text{-}ZnO + h\nu \rightarrow Ta\text{-}ZnO\ (e^- + h^+) \qquad (6)$$

$$e^- + O_2 \rightarrow {}^{\bullet}O_2^- \qquad (7)$$

$$h^+ + H_2O \rightarrow {}^{\bullet}OH + H^+ \qquad (8)$$

$$e^-, h^+, {}^{\bullet}O_2^-, {}^{\bullet}OH + MB \rightarrow$$
$$\text{degradation products} + CO_2 + H_2O \qquad (9)$$

4. Conclusion

Ta-doped ZnO nanorods were successfully synthesized by a hydrothermal method at different hydrothermal temperatures. This study demonstrated that Ta-doping affects the optical and photocatalytic properties of ZnO. The band gap of Ta-doped ZnO (2.92 eV) decreases compared to undoped ZnO (3.07 eV). Therefore, the nanorods can absorb light with a wavelength of 425 nm. Ta-doping improved the MB degradation efficiency under visible light due to an increase in the oxygen hole defect, which has a significant impact on decreasing the rate that the electrons and holes recombine. Blue light emission peaks identified these defects in the photoluminescence and XPS spectra. Notable, the results showed that hydrothermal temperature significantly influences the structure, morphology, photoelectrical properties, and photocatalyst of Ta-doped ZnO nanorods. A high hydro-thermal temperature (*i.e.*, 170 °C) increases the autogenous pressure, which is thermodynamically favorable for forming Ta_2O_5 and $ZnTa_2O_6$ phases. That causes larger rods and broken rods to form. As a result, the optimal hydrothermal temperature for synthesized Ta-doped ZnO nanorods is 150 °C for the pho-todegradation of MB.

Author contributions

Luu Thi Viet Ha: methodology, writing – original draft, valida-tion, writing – review & editing, project administration. Dao Ngoc Nhiem: data curation, resources, supervision. Nguyen Van Cuong: investigation, resources. Pham Hoang Ai Le: data curation, software. Nguyen Quang Bac: investigation, resources. Dang Huu Phuc: writing – review & editing.

Conflicts of interest

The authors declare that they have no known competing inter-ests that could have appeared to influence the work reported in this paper.

References

1 Ü. Özgür, Y. I. Alivov, C. Liu, A. Teke, M. A. Reshchikov, S. Doğan, V. Avrutin, S. J. Cho and H. Morko, *J. Appl. Phys.*, 2005, **98**, 1–103.

2 D. Segets, J. Gradl, R. K. Taylor, V. Vassilev and W. Peukert, *ACS Nano*, 2009, **3**, 1703–1710.

3 A. Kolodziejczak-Radzimska and T. Jesionowski, *Materials*, 2014, **7**, 2833–2881.

4 D. Nohavica and P. Gladkov, *Olomouc, Czech Republic, EU*, 2010, **10**, 12–14.

5 H. Hamrayev and K. Shameli, *IOP Conf. Ser.: Mater. Sci. Eng.*, 2021, **1051**, 012088.

6 A. A. Barzinjy, S. Hamad and H. Azeez, *Jordan J. Phys.*, 2020, **13**, 123–135.

7 M. N. Chong, B. Jin, C. W. K. Chow and C. Saint, *Water Res.*, 2010, **44**, 2997–3027.

8 T. Khalafi, F. Buazar and K. Ghanemi, *Sci. Rep.*, 2019, **9**, 1–10.

9 R. Qiu, D. Zhang, Y. Mo, L. Song, E. Brewer, X. Huang and Y. Xiong, *J. Hazard. Mater.*, 2008, **156**, 80–85.

10 S. K. Kansal, M. Singh and D. Sud, *J. Hazard. Mater.*, 2007, **141**, 581–590.

11 A. N. C. O. Cambrussi, A. Í. S. Morais, A. D. M. Neris, J. A. Osajima, E. C. D. S. Filho and A. B. Ribeiro, *Matéria (Rio de Janeiro)*, 2019, **24**, DOI: **10.1590/s1517-707620190004.0807**.

12 C. S. Chen, X. D. Xie, T. G. Liu, L. W. Lin, J. C. Kuang, X. L. Xie, L. J. Lu and S. Y. Cao, *J. Nanopart. Res.*, 2012, **14**, 1–8.

13 C. S. Chen, T. G. Liu, L. W. Lin, X. D. Xie, X. H. Chen, Q. C. Liu, B. Liang, W. W. Yu and C. Y. Qiu, *J. Nanopart. Res.*, 2013, **15**, 1–9.

14 G. Sapkota, K. Gryczynski, R. McDougald, A. Neogi and U. Philipose, *J. Electron. Mater.*, 2012, **41**, 2155–2161.

15 T. Y. Ko, M. H. Tsai, C. S. Lee and K. W. Sun, *J. Nanopart. Res.*, 2012, **14**, 1–12.

16 J. Z. Kong, A. D. Li, H. F. Zhai, Y. P. Gong, H. Li and D. Wu, *J. Solid State Chem.*, 2009, **182**, 2061–2067.

17 J. Z. Kong, A. D. Li, X. Y. Li, H. F. Zhai, W. Q. Zhang, Y. P. Gong, H. Li and D. Wu, *J. Solid State Chem.*, 2010, **183**, 1359–1364.

18 P. Pascariu, C. Cojocaru, N. Olaru, P. Samoila, A. Airinei, M. Ignat, L. Sacarescu and D. Timpu, *J. Environ. Manage.*, 2019, **239**, 225–234.

19 B. Chouchene, T. ben Chaabane, L. Balan, E. Girot, K. Mozet, G. Medjahdi and R. Schneider, *Beilstein J. Nanotechnol.*, 2016, **7**, 1338–1349.

20 E. Cerrato, C. Gionco, I. Berruti, F. Sordello, P. Calza and M. C. Paganini, *J. Solid State Chem.*, 2018, **264**, 42–47.

21 P. Pandey, R. Kurchania and F. Z. Haque, *Opt. Spectrosc.*, 2015, **119**, 666–671.

22 K. C. Barick, S. Singh, M. Aslam and D. Bahadur, *Microporous Mesoporous Mater.*, 2010, **134**, 195–202.

23 S. Chakma and V. S. Moholkar, *Ultrason. Sonochem.*, 2015, **22**, 287–299.

24 J. Iqbal, X. Liu, H. Zhu, Z. B. Wu, Y. Zhang, D. Yu and R. Yu, *Acta Mater.*, 2009, **57**, 4790–4796.

25 G. Thennarasu and A. Sivasamy, *Powder Technol.*, 2013, **250**, 1–12.

26 V. Herrera, T. Díaz-Becerril, E. Reyes-Cervantes, G. García-Salgado, R. Galeazzi, C. Morales, E. Rosendo, A. Coyopol, R. Romano and F. G. Nieto-Caballero, *Crystals*, 2018, **8**, 395.

27 R. Althaf and A. M. Ashok, *J. Appl. Phys.*, 2020, **128**, 165110.

28 Y. Wu, C. Li, M. Li, H. Li, S. Xu, X. Wu and B. Yang, *Ceram. Int.*, 2016, **42**, 10847–10853.

29 S. Mageswari and B. Palanivel, *Curr. Smart Mater.*, 2019, **4**, 45–58.

30 B. L. Guo, P. Han, L. C. Guo, Y. Q. Cao, A. D. Li, J. Z. Kong, H. F. Zhai and D. Wu, *Nanoscale Res. Lett.*, 2015, **10**, 1–10.

31 B. I. Arias-Serrano, W. Xie, M. H. Aguirre, D. M. Tobaldi, A. R. Sarabando, S. Rasekh, S. M. Mikhalev, J. R. Frade, A. Weidenkaff and A. V. Kovalevsky, *Materials*, 2019, **12**, 2057.

32 S. Pat, R. Mohammadigharehbagh and Ş. Korkmaz, *Opt. Quantum Electron.*, 2021, **53**, 1–11.

33 B.-L. Guo, P. Han, L.-C. Guo, Y.-Q. Cao, A.-D. Li, J.-Z. Kong, H.-F. Zhai and D. Wu, *Nanoscale Res. Lett.*, 2015, **10**, 336.

34 P. Babaei, J. Safai-Ghomi and S. Rashki, *Ceram. Int.*, 2022, **48**, 8359–8373.

35 B.-L. Guo, P. Han, L.-C. Guo, Y.-Q. Cao, A.-D. Li, J.-Z. Kong, H.-F. Zhai and D. Wu, *Nanoscale Res. Lett.*, 2015, **10**, 336.

36 T. Liu, L. Wang, X. Lu, J. Fan, X. Cai, B. Gao, R. Miao, J. Wang and Y. Lv, *RSC Adv.*, 2017, **7**, 12292–12300.

37 L. T. V. Ha, L. M. Dai, D. T. Lim, D. N. Nhiem and N. N. Pham, *J. Chin. Chem. Soc.*, 2020, **67**, 1631–1643.

38 S. H. Chen, Y. S. Jiang and H. Y. Lin, *ACS Omega*, 2020, **5**, 8927–8933.

39 D. Richard, M. Romero and R. Faccio, *Ceram. Int.*, 2018, **44**, 703–711.

40 S. Gandla, S. R. Gollu, R. Sharma, V. Sarangi and D. Gupta, *Appl. Phys. Lett.*, 2015, **107**, 152102.

41 N. Kannadasan, N. Shanmugam, S. Cholan, K. Sathishkumar, G. Viruthagiri and R. Poonguzhali, *Mater. Charact.*, 2014, **97**, 37–46.

42 J. Wen, H. Guo, X. Ma, Z. Wei, X. He, L. Zhang, B. Li, T. Wang and Y. Cheng, *Catal. Sci. Technol.*, 2020, **10**, 3739–3747.

43 M. Montero-Muñoz, J. E. Ramos-Ibarra, J. E. Rodríguez-Páez, M. D. Teodoro, G. E. Marques, A. R. Sanabria, P. C. Cajas, C. A. Páez, B. Heinrichs and J. A. H. Coaquira, *Appl. Surf. Sci.*, 2018, **448**, 646–654.

44 P. Ghasemipour, M. Fattahi, B. Rasekh and F. Yazdian, *Sci. Rep.*, 2020, **10**, 4414.

45 S. Xiao, D. Zhang, D. Pan, W. Zhu, P. Liu, Y. Cai, G. Li and H. Li, *Nat. Commun.*, 2019, **10**, 1570.

46 S. J. Park, G. S. Das, F. Schütt, R. Adelung, Y. K. Mishra, K. M. Tripathi and T. Y. Kim, *NPG Asia Mater.*, 2019, **11**, 8.

47 E. A. Davis and N. F. Mott, *Philos. Mag.*, 1970, **22**, 903–922.

48 B. D. Viezbicke, S. Patel, B. E. Davis and D. P. Birnie, *Phys. Status Solidi B*, 2015, **252**, 1700–1710.

49 K. Irshad, M. T. Khan and A. Murtaza, *Phys. B*, 2018, **543**, 1–6.

50 R. K. Biroju and P. K. Giri, *J. Appl. Phys.*, 2017, **122**, 044302.

51 A. Janotti and C. G. van de Walle, *Rep. Prog. Phys.*, 2009, **72**, 126501.

52 J. L. Cervantes-López, R. Rangel, J. Espino, E. Martínez, R. García-Gutiérrez, P. Bartolo-Pérez, J. J. Alvarado-Gil and O. E. Contreras, *Appl. Phys. A: Mater. Sci. Process.*, 2017, **123**, 1–14.

53 B. I. Kharisov, O. V. Kharissova and U. O. Mendez, *The Development and Application of Microwave Heating*, InTech, 2012, vol. 5, pp. 107–140.

54 T. K. Pathak, E. Coetsee-Hugo, H. C. Swart, C. W. Swart and R. E. Kroon, *Mater. Sci. Eng. B: Solid-State Mater. Adv. Technol.*, 2020, **261**, 114780.

55 J. Z. Kong, A. D. Li, X. Y. Li, H. F. Zhai, W. Q. Zhang, Y. P. Gong, H. Li and D. Wu, *J. Solid State Chem.*, 2010, **183**, 1359–1364.

56 C. Rodwihok, D. Wongratanaphisan, T. van Tam, W. M. Choi, S. H. Hur and J. S. Chung, *Appl. Sci.*, 2020, **10**, 1697.

57 W. H. Koppenol, D. M. Stanbury and P. L. Bounds, *Free Radicals Biol. Med.*, 2010, **49**, 317–322.